

Linearization of the effect of slit function changes for improving OMI ozone profile retrievals

Juseon Bak^{a,*}, Xiong Liu^a, Kang Sun^b, Kelly Chance^a, Jae-Hwan Kim^c

^a*Harvard-Smithsonian Center for Astrophysics, Cambridge, MA, USA*

^b*Research and Education in eNergy, Environment and Water Institute, University at Buffalo, Buffalo, NY, USA*

^c*Atmospheric Science Department, Pusan National University, Busan, Korea*

*Corresponding Author (juseon.bak@cfa.harvard.edu)

Abstract

We introduce a method that accounts for errors caused by the slit function in an optimal estimation based spectral fitting process to improve ozone profile retrievals from the Ozone Monitoring Instrument (OMI) ultraviolet measurements (270-330 nm). Previously, a slit function was parameterized as a standard Gaussian by fitting the Full Width at Half Maximum (FWHM) of the slit function from climatological OMI solar irradiances. This cannot account for the temporal variation of slit function in irradiance, the intra-orbit changes due to thermally-induced change and scene inhomogeneity, and potential differences in the slit functions of irradiance and radiance measurements. As a result, radiance simulation errors may be induced due to convolving reference spectra with incorrect slit functions. To better represent the shape of the slit functions, we implement a more generic super Gaussian slit function with two free parameters (slit width and shape factor); it becomes standard Gaussian when the shape factor is fixed to be 2. The effects of errors in slit function parameters on radiance spectra, referred as “Pseudo Absorbers (PAs)”, are linearized by convolving high-resolution cross sections or simulated radiances with the partial derivatives of the slit function with respect to the slit parameters. The PAs are included in the spectral fitting scaled by fitting coefficients that are iteratively adjusted as elements of the state vector along with ozone and other fitting parameters. The fitting coefficients vary with cross-track and along-track pixels and show sensitivity to heterogeneous scenes. The PA spectrum is quite similar in the Hartley band below 310 nm for both standard and super Gaussians, but is more distinctly structured in the Huggins band above 310 nm with the use of super Gaussian slit functions. Finally, we demonstrate that some spikes of fitting residuals are slightly smoothed by accounting for the slit function errors. Comparisons with ozonesondes demonstrate noticeable

29 improvements when using PAs for both standard and super Gaussians, especially for reducing the
30 systematic biases in the tropics and mid-latitudes (mean biases of tropospheric column ozone reduced from
31 $-1.4 \sim 0.7$ DU to $0.0 \sim 0.4$ DU) and reducing the standard deviations of tropospheric ozone column
32 differences at high-latitudes (by 1 DU for the super Gaussian). Including PAs also makes the retrievals
33 consistent between standard and super Gaussians. This study corroborates the slit function differences
34 between radiance and irradiance demonstrating that it is important to account for such differences in the
35 ozone profile retrievals.

36

37 **1. Introduction**

38 The fitting of measured spectra to simulated spectra is the most basic concept for analysis of the Earth's
39 atmospheric constituents from satellite measurements. Therefore, accurate calibration and simulation of
40 measurements are essential for the successful retrieval of atmospheric constituents. The knowledge of the
41 instrumental spectral response function (ISRF) or slit function could affect the accuracies of both calibration
42 and simulation, as it is required for the convolution of a high-resolution reference spectrum to instrument's
43 spectral resolution in the wavelength calibration and for the convolution of high-resolution absorption cross
44 section spectra or simulated radiance spectra in the calculation of radiance at instrumental resolution.
45 Compared to other trace gases, the retrieval of ozone profiles can be more susceptible to the accuracy of
46 ISRFs due to the large spectral range, where the radiance spans a few orders of magnitude and to the fact
47 that the spectral fingerprint for the tropospheric ozone is primarily provided by the 310-330 nm absorption
48 features residing in the temperature-dependent Huggins bands. Therefore, the efforts to characterize and
49 verify the ISRFs have preceded the analyses of ozone profiles from satellite and aircraft measurements (Liu
50 et al., 2005, 2010; Cai et al., 2012; Liu et al., 2015; Sun et al. 2017; Bak et al., 2017).

51 For space-borne instruments, ISRFs are typically characterized as a function of the detector dimensions
52 using a tunable laser source prior to the launch (Dirksen et al., 2006; Liu et al., 2015; van Hees et al., 2018)
53 and directly used in ozone profile retrievals (e.g., Kroon et al., 2011; Mielonen et al., 2015; Fu et al., 2013;
54 2018). However, the preflight measured ISRFs could be inconsistent with those after launch due to the
55 orbital movement and the instrument temperature change (Beirle et al., 2017; Sun et al., 2017). Therefore,
56 the post-launch ISRFs have been fitted from the preflight ones (e.g., Bak et al., 2017; Sun et al., 2017) or
57 parameterized through a cross-correlation of the measured solar irradiance to a high-resolution solar
58 spectrum (Caspar and Chance, 1997), assuming Gaussian-like shapes (e.g., Liu et al. 2005; 2010). The
59 direct retrieval of the ISRFs from radiances has not typically been done due to the complication of taking
60 the atmospheric trace gas absorption and Ring effect into account in the cross-correlation procedure and

61 the slow-down of the fitting process. However, slit function differences between radiance and irradiance
62 could exist due to scene heterogeneity, differences in stray light between radiance and irradiance, and intra-
63 orbit instrumental changes (such as instrument temperature change) (Beirle et al., 2017; Sun et al., 2017).
64 In addition, using temporally invariant slit functions derived from climatological solar spectra in the
65 retrievals could cause the long-term trend errors if instrument degradation occurs. Therefore, there is room
66 for improving our trace gas retrievals by accounting for the effects of the different ISRFs between radiance
67 and irradiance on the spectral fitting on a pixel-to-pixel basis. The “Pseudo Absorber (PA)” is a common
68 concept in spectral fitting to account for the effect of physical phenomena that are difficult or
69 computationally demanding to be simulated in radiative transfer calculations, like spectral misalignments
70 (shift and stretch) between radiance and irradiance, Ring effect, spectral undersampling, and additive stray-
71 light offsets. The pseudo absorption spectrum can be derived from a finite-difference scheme (e.g. Azam and
72 Richter, 2015) or a linearization scheme via a Taylor expansion (e.g. Beirle et al., 2013; 2017); the latter
73 approach is more efficient than the former one, but less accurate because only the first term of the Taylor
74 series is typically taken into account for simplicity. Beirle et al. (2013) introduced a linearization scheme
75 to account for spectral misalignments between radiance and irradiance and then included them as a pseudo-
76 absorber in DOAS-based NO₂ and BrO fittings. Similarly, Beirle et al. (2017) linearized the effect of the
77 change of the ISRF parameterized as a super Gaussian on GOME-2 solar irradiance spectra to characterize
78 the slit function change over time and wavelength. Sun et al. (2017) derived on-orbit slit functions from
79 solar irradiance spectra measured by the Ozone Monitoring Instrument (OMI) (Levelt et al., 2006) assuming
80 standard Gaussian, super Gaussian, and preflight ISRFs with adjusted widths. The derived on-orbit slit
81 functions, showing significant cross-track dependence that cannot be represented by preflight ISRFs,
82 substantially improve the retrievals by the Smithsonian Astrophysical Observatory (SAO) ozone profile
83 algorithm. However, it is not fully understood why the use of super Gaussian or stretched preflight functions,
84 which are supposed to better model the OMI spectra as indicated by smaller mean fitting residuals, does
85 not improve the retrievals over the use of standard Gaussian especially in the standard deviations of the
86 differences with relative to ozonesonde observations. This study suggests that the slit functions derived
87 from solar spectra might not fully represent those in radiance spectra.

88 As such, the objective of this paper is to expand the slit function linearization proposed by Beirle et
89 al. (2017) into the optimal estimation based spectral fitting of the SAO ozone profile algorithm. The slit
90 function linearization is used to account for the radiative transfer calculation errors caused by the slit
91 functions differences between radiance and irradiance on a pixel-by-pixel basis, and ultimately to improve
92 OMI ozone profile retrievals. This paper is organized as follows: after a mathematical description of the
93 linearization of slit function changes using the generic super Gaussian function, we introduce their practical
94 application in an optimal estimation based spectral fit procedure (Section 2). This linearization scheme is

95 implemented differently, depending on the simulation scheme of measured spectra using high resolution or
 96 effective cross section data, respectively. Section 3 characterizes the derived pseudo absorber spectra, along
 97 with evaluations of ozone profile retrievals using independent ozonesonde observations as a reference
 98 dataset. Finally, the summary of this study is given in Section 4.

99 2. Method

100 2.1 Super Gaussian linearization

101 The slit function parameterization and linearization are briefly summarized as in Beirle et al. (2017),
 102 focusing on what we need to derive the pseudo absorbers in the terms of the optimal estimation based fitting
 103 process. The slit function can be parameterized with the slit width w , and shape factor k assuming the
 104 supper Gaussian, S as:

$$105 \quad S(\Delta\lambda) = A(w, k) \times \exp\left[-\left|\frac{\Delta\lambda}{w}\right|^k\right], \quad (1)$$

106 where $A(w, k)$ is $\frac{k}{2\sigma_g\Gamma(\frac{1}{w})}$ with Γ representing the gamma function. This equation allows many forms of
 107 distributions by varying k : the top-peaked function ($k < 2$), the standard Gaussian function ($k = 2$), and the
 108 flat-topped function ($k > 2$). w is converted to the Full Width at Half Maximum (FWHM) via the relationship
 109 of $\text{FWHM} = 2\sqrt[k]{\ln 2} w$. We investigate the impact of including one more slit parameter k on the OMI ISRF
 110 fitting results over the standard Gaussian using OMI daily solar measurements. As an example, time-series
 111 (2005-2015) of the fitted slit width and shape factor in 310-330 nm are displayed in Figure 1.a. The FWHM
 112 and shape factor of the super Gaussian function is on average 0.44 nm and 2.9, respectively, while the
 113 FWHM of the standard Gaussian is 0.395 nm. The sharp change and random-noise of these derived slit
 114 function parameters might be influenced by the decreasing signal-to-noise ratio (SNR) of solar spectra later
 115 in the OMI mission and radiometric errors in solar irradiance due to the row anomaly (Sun et al., 2017).
 116 Figure 1.b illustrates the high wavelength stability (0.003 nm) in the OMI mission, verifying that better
 117 calibration stability is performed with super Gaussian slit functions as abnormal deviations of wavelength
 118 shifts are derived with standard Gaussian slit functions.

119 The effect of changing the slit parameters p on the slit function can be linearized by the first-order
 120 Taylor expansion approximation around $S_0 = S(p_0)$:

$$121 \quad \Delta S = S - S_0 \approx \Delta p \frac{\partial S}{\partial p}, \quad (2)$$

122 and thus the effect of changes of S on the convolved high-resolution spectrum can be parameterized as

123
$$\Delta I = I - I_o = S \otimes I_h - S_o \otimes I_h = \Delta S \otimes I_h, (3)$$

124 where the convolved spectrum is $I = S \otimes I_h$. Consequently, the partial derivatives of I with respect to slit
 125 parameters p are defined as

126
$$\frac{\partial I}{\partial p} = \frac{\partial S}{\partial p} \otimes I_h. (4)$$

127 Beierle et al. (2017) refers to $\frac{\partial I}{\partial p} J_p$ as J_p , “resolution correction spectra (RCS)”. In Figure 2, we present
 128 an example of J_p over the typical ozone profile fitting range (270-330 nm) through the convolution of high-
 129 resolution ozone cross sections (δ_h) with the derivatives of the super Gaussian ($\frac{\partial S}{\partial p}$). The baseline S_o is
 130 defined with $w=0.26$ nm and $k=2.6$, which are averaged parameters from climatological OMI solar
 131 irradiance spectra in the UV2 band (310-330 nm). Note that this w value corresponds to a FWHM of 0.45
 132 nm. The change of the assumed OMI slit function causes a highly structured spectral response over the
 133 whole fitting window. However, the relative magnitude of the responses with respect to both slit parameters
 134 is more distinct in the Huggins band (>310 nm) where narrow absorption features are observed as shown
 135 in Figure 2.a. An anti-correlation (-0.92) is found between $\frac{\partial \ln \delta}{\partial w}$ and $\frac{\partial \ln \delta}{\partial k}$ while the response of the unit
 136 change of the slit width to the convolved spectrum is dominant against that of the shape factor.

137 **2.2 Implementation of the slit function linearization in the SAO ozone profile algorithm**
 138

139 In Beirle et al. (2017) a slit function linearization was implemented only to fit solar irradiances from
 140 GOME-2. We implement the slit function linearization to fit radiances in the SAO ozone profile algorithm
 141 (Liu et al. 2010), which is routinely being performed to produce the OMI PROFOZ product
 142 (<https://avdc.gsfc.nasa.gov/index.php?site=1389025893&id=74>). Two spectral windows (270-309 nm in
 143 the UV1 band and 312-330 nm in the UV2 band) are employed to retrieve ozone profiles from OMI BUW
 144 measurements. To match the different spatial resolutions between UV1 and UV2 bands, every two cross-
 145 track pixels are averaged for UV2 band, resulting into 30 positions with the spatial resolution of 48 km
 146 (across-track) \times 13 km (along-track) at nadir position. Partial ozone columns at 24 layers between the
 147 surface and 60 km are iteratively estimated toward minimizing the fitting residuals between measured and
 148 simulated radiances and simultaneously between a priori and estimated ozone values using the optimal
 149 estimation inversion method. A priori ozone information is taken from a tropopause-based (TB) ozone
 150 profile climatology (Bak et al., 2013). The Vector Linearized Discrete Ordinate Radiative Transfer model
 151 (VLIDORT; Spurr, 2008) is used to simulate the radiances and their derivatives with respect to geophysical
 152 parameters. The radiance calculation is made for the Rayleigh atmosphere, where the incoming sunlight is
 153 simply absorbed by ozone and other trace gases, scattered by air molecules, and reflected by surfaces/clouds

154 assumed as a Lambertian surface. Besides these, other physical phenomena are treated as PAs to the spectral
 155 response such as Ring effect, additive offset, and spectral shifts due to misalignments of radiance relative
 156 to irradiance and ozone cross sections. In the SAO algorithm, these PAs are derived using finite differences
 157 of the radiances with and without perturbation to a phenomenon, except for the Ring spectrum that is
 158 calculated using a first-order single scattering rotational Raman scattering model (Sioris and Evans, 2000).
 159 In this paper, we introduce new PAs to account for the radiance simulation errors caused by the slit function
 160 errors. The OMI ISRFs have been parameterized as a standard Gaussian from climatological OMI solar
 161 irradiances for each UV1 and UV2 band and thereby these PAs could take into account the spectral fitting
 162 responses caused by temporal variations of the slit function. This ozone fitting procedure uses ISRFs to
 163 convolve high resolution absorption spectra, taken from Brion et al. (1993) for ozone absorption cross
 164 sections and Wilmouth et al. (1999) for BrO absorption cross sections. In DOAS analysis, the pseudo
 165 absorber is defined as $\frac{\partial S}{\partial p} \otimes \sigma_h$ (σ_h is a high-resolution absorption cross section), which could be calculated
 166 at a computationally low-cost. In our optimal estimation based ozone profile retrievals, it is conceptually
 167 defined as $\frac{\partial S}{\partial p} \otimes I_h$ (I_h is a high-resolution simulated radiance), which is computationally very expensive
 168 because of on-line radiative calculation for a ~ 60 nm wide fit window on the spatial pixel-to-pixel basis.
 169 We now introduce how to implement the slit function linearization to derive the derivatives of the OMI
 170 radiances with respect to slit function changes in two different radiative transfer approaches used in the
 171 SAO ozone profile algorithm, i.e., the effective cross section approach in Liu et al (2010) and the updated
 172 high-resolution convolution approach described in Kim et al. (2013), respectively.

173 In Liu et al (2010), VLIDORT simulates the radiances at OMI spectral grids (λ_{omi}) using effective
 174 cross sections that are produced by convolving high-resolution cross sections with the OMI ISRFs.
 175 Therefore, we apply a similar convolution process of matching the high-resolution cross section spectra
 176 with OMI spectra to derive the partial derivative of σ_x with respect to slit parameter, p as follows:

$$177 \quad \frac{\partial \sigma_x}{\partial p} = \frac{\partial S}{\partial p} \otimes \sigma_{x,h}, \quad (5)$$

178 where $\sigma_{x,h}$ is a high-resolution absorption spectrum for ozone or BrO. Due to the dominant absorption of
 179 O_3 over BrO, the derivative of the BrO cross section with respect to p is neglected here. This partial
 180 derivative of ozone is then converted to the partial derivative of radiance through the chain rule with the
 181 analytical ozone weighting function ($\frac{d \ln I}{d O_3}$), calculated from VLIDORT, as follows:

$$182 \quad \frac{\partial \ln I}{\partial p} = \frac{\partial \ln I}{\partial O_3} \frac{\partial \sigma}{\partial p} \frac{O_3}{\sigma}. \quad (6)$$

184 This simulation process is hereafter referred to as “effective resolution cross section (ER) simulation”.

185 As described in Kim et al. (2013), the radiative transfer calculation in the SAO ozone profile algorithm
 186 has been performed using high-resolution extinction spectra at the optimized sampling intervals for
 187 resolving the ozone absorption features, which are a ~1.0 nm below 300 nm and ~0.4 nm above 300 nm.
 188 These sampling intervals are coarser than actual OMI sampling grids with approximately half the number
 189 of wavelengths. The coarser sampled simulated radiances are then interpolated to a fine grid of 0.05 nm
 190 assisted by the weighting functions with respect to absorption and Rayleigh optical depth:

$$191 \quad I(\lambda_h) = I(\lambda_c) + \frac{\partial I(\lambda_c)}{\partial \Delta_l^{gas}} \left(\Delta_l^{gas}(\lambda_h) - \Delta_l^{gas}(\lambda_c) \right) + \frac{\partial I(\lambda_c)}{\partial \Delta_l^{ray}} \left(\Delta_l^{ray}(\lambda_h) - \Delta_l^{ray}(\lambda_c) \right), \quad (7)$$

192 where Δ_l^{gas} and Δ_l^{ray} are the optical thickness (the product of cross section and layer column density) at
 193 each layer for trace gas absorption and Rayleigh scattering, respectively. The convolution is then applied
 194 to these simulated high-resolution radiances, $I(\lambda_h)$ with assumed slit functions and derivatives, respectively,
 195 and thereby $I(\lambda_{omi})$ and $\frac{\partial \ln I}{\partial p}$ is calculated. This simulation process is hereafter referred to as “high-
 196 resolution cross section (HR) simulation.” The ER simulation is more commonly implemented in trace gas
 197 retrievals in the UV and visible, but the HR simulation allows for more accurate fitting residuals, to better
 198 than 0.1 % (Kim et al., 2013) as well as shorter computation time. $\frac{\partial \ln I}{\partial p}$ is scaled by the fitting coefficients,
 199 Δp , to account for the actual size of the spectral structures caused by the slit function differences between
 200 radiance and irradiance spectra. The “pseudo absorber (PA)” for the super Gaussian slit function
 201 linearization is expressed as:

$$202 \quad PA = \partial \ln I = \frac{\partial \ln I}{\partial k} \Delta k + \frac{\partial \ln I}{\partial w} \Delta w. \quad (8)$$

203 In the form of the logarithm of normalized radiance, PA is physically related to the optical depth change
 204 $\Delta \tau$. Figure 3 compares the partial derivatives of radiances to slit parameters, $\frac{d \ln I}{d p}$ in HR and ER simulations.
 205 Little difference is found even though convolution error for ozone cross sections is only accounted for in
 206 the ER simulation due to the overwhelming impact of ozone cross section convolution errors over other
 207 cross section data. The amplitude of $\frac{d \ln I}{d p}$ varies with different satellite pixels (e.g., ozone profile shape,
 208 geometry, and cloud/surface property), but the spectral peak positions do not change because they arise
 209 from the errors due to the convolution process of high-resolution absorption cross-sections dominated by
 210 ozone. It should be noted that these spectral structures are weakly correlated with the partial derivatives of
 211 radiances with respect to other state vectors (ozone, BrO, cloud fraction, surface albedo, radiance/irradiance
 212 shift, radiance/ozone cross section shift, Ring, mean fitting residual scaling factor) within ± 0.3 and ± 0.1
 213 in the UV 1 and UV 2, respectively.

214 Furthermore, this linearization process can be formulated with n-order polynomial fitting parameters
215 (Δp_i) to account for the wavelength-dependent change of the slit parameters around a central wavelength
216 $\bar{\lambda}$, which is expressed as

$$217 \quad PA = \frac{\partial \ln I}{\partial k} \sum_{i=1}^n \Delta k_i \cdot (\lambda - \bar{\lambda})^{n-1} + \frac{\partial \ln I}{\partial w} \sum_{i=1}^n \Delta w_i \cdot (\lambda - \bar{\lambda})^{n-1}. \quad (9)$$

218

219 **3. Results and Discussion**

220 We characterize the effect of including the PA ($\frac{\partial \ln I}{\partial p} \cdot \Delta p$) on ozone profile retrievals using both Super
221 Gaussian and standard Gaussian slit functions. Hereafter, the correction spectrum ($\frac{\partial \ln I}{\partial p}$) is derived using the
222 HR simulation. The PA coefficient (Δp_i) (one for each channel and for each order) is included as part of
223 the state vector to be iteratively and simultaneously retrieved with ozone. The a priori value is set to be zero
224 for all fitting coefficients, while the a priori error is set to be 0.1, empirically. We should note that the
225 empirical “soft calibration” is applied to OMI radiances before the spectral fitting, in order to eliminate the
226 wavelength and cross-track dependent systematic biases, due to the interference of the PA coefficients with
227 systematic measurement errors during the fitting process.

228 **3.1 Characterization of the pseudo absorbers in ozone fitting procedure**

229 Figure 4 displays how the zero-order PA coefficients (Δp) vary within one orbit when slit functions are
230 assumed as standard and Super Gaussians, respectively, along with variation of cloud fraction, surface
231 albedo, and cloud pressure from the retrievals. These retrieved coefficients physically represent the
232 deviation of ISRFs in radiances from those in solar measurements. We normalize them with the slit
233 parameters derived from OMI solar irradiances for a better interpretation. Cross-track dependent features
234 are shown in slit width. The relative change of the slit width is more distinct in the UV1 band than in the
235 UV2 band, whereas the change of the shape factor is more distinct in the UV2 band. The UV2 slit widths
236 increase typically within 5 % over the given spatial domain. However, the UV1 slit widths increase from
237 10 % at most pixels up to 50 % at off-nadir positions in the high latitudes, which might be caused by stray
238 light differences between radiance and irradiance and intra-orbit instrumental changes. An abnormal change
239 of the UV1 slit parameters due to the scene heterogeneity is detected at the along-track scan positions of
240 ~300 and 900, respectively, where upper-level clouds are present. The UV2 shape factor changes show a
241 coherent sensitivity to bright surfaces under clear-sky condition over the northern high latitudes. Fitting
242 coefficients for the standard Gaussian show a quite similar spatial variation for the UV1 slit width

243 (correlation = ~ 0.98), but an anti-correlation of ~ -0.62 for the UV2 slit width compared to those for Super
244 Gaussian due to the interference between shape factor and slit width.

245 Examples of the PAs (eq. 9) are illustrated in Figure 5 when (a) zero and (b) first-order polynomial
246 coefficients are fitted, respectively. In the UV1 range, the sum of PAs multiplied by corresponding
247 coefficients, regardless of which Gaussian is assumed as slit function, is very similar because the spectral
248 structure caused by the slit width change is dominant. It implies that OMI ISRFs in the UV1 band are
249 similar to the standard Gaussian, for both radiance and irradiance measurements, consistent with the pre-
250 launch characterization (Dirksen et al., 2006). However, in the UV2 range, the spectral structures are
251 generated by the shape factor change rather than the slit width change and therefore PAs show noticeable
252 discrepancies for different Gaussian assumptions. Our results indicate that the PA for the shape factor
253 change is required to adjust the spectral structures due to the differences in the slit functions between
254 radiance and irradiance over the UV2 band. In the case of the wavelength dependent PA coefficient fit, the
255 impact of first-order PAs on OMI radiances is relatively visible in the wavelength range of 300-310 nm.
256 This result is physically consistent with the wavelength dependent property shown in the slit parameters
257 derived from OMI irradiances as shown in Figure 6 where slit parameters are characterized in 10-pixel
258 increments assuming the super Gaussian slit function. In UV1, the slit widths plotted as FWHM slightly
259 decrease by ~ 0.1 nm at shorter wavelengths than 288 nm, but vary more sharply by up to ~ 0.2 nm at longer
260 wavelengths. Compared to slit widths, the wavelength dependences of the shape factors are less noticeable,
261 except at boundaries of the window. In the UV2 window, both slit width and shape factor are highly
262 invariant.

263 **3.2 Impact of including pseudo absorbers on ozone profile retrievals**

264 Figures 7 to 9 evaluate the impact of including zero-order PAs on ozone profile retrievals. Figure 7
265 illustrates how different assumptions in the slit functions affect the ozone profile retrievals with respect to
266 the retrieval sensitivity and the fitting accuracy from the case shown in Figure 4. In this figure, the Degrees
267 of Freedom for Signal (DFS) represents the independent pieces of ozone information available from
268 measurements, which typically decreases as ozone retrievals are further constrained by other fitting
269 variables. The reduced DFS values ($< 5\%$) imply that the ozone retrievals are correlated slightly with PAs.
270 The fitting accuracy is assessed as the root mean square (RMS) of the relative differences (%) between
271 measured and calculated radiances over the UV1 and UV2 ranges, respectively. Including the PAs makes
272 little difference in the UV1 fitting residuals for most of individual pixels (1-5%), but significantly reduces
273 residuals in the UV2 range. The adjusted amounts of the residuals with PAs are generally larger when
274 assuming super Gaussian slit functions. This comes from different assumptions for slit functions in deriving
275 soft calibration spectra, where slit functions were parameterized as standard Gaussians. Therefore, applying

276 soft calibration to OMI spectra entails somewhat artificial spectral structures if ISRFs are assumed as super
277 Gaussian in ozone retrievals, and hence the impact of PAs on the spectral fitting becomes more considerable.
278 Figure 8 compares how the spectral residuals are adjusted with PAs when soft calibration is turned on and
279 off, respectively. Using super Gaussians causes larger amplitudes of the spectral fitting residuals than using
280 standard Gaussians, if soft calibration is turned on and PAs are excluded. On the other hand, some residuals
281 are reduced and more broadly structured if soft calibration is turned off. Including PAs eliminates or reduces
282 some spikes of fitting residuals as well as improves the consistency of the fitting accuracy between using
283 standard and super Gaussians at wavelengths above 300 nm.

284 The benefit of this implementation on ozone retrievals is further assessed through comparison with
285 Electrochemical Concentration Cell (ECC) ozonesondes collected from the WOUDC (<https://woudc.org/>)
286 and SHADOZ (<https://tropo.gsfc.nasa.gov/shadoz/>) networks. This evaluation is limited to the period of
287 2005 through 2008 to avoid interferences with row-anomaly effects appearing in 2007 and becoming
288 serious in early 2009 (Schenkeveld, et al 2017). We select 13 SHADOZ sites in the tropics and 38 WOUDC
289 sites in the northern mid/high latitudes. The collocation criteria is within $\pm 1^\circ$ in latitude and longitude
290 and within 12 hours in time. For comparison, high-vertical resolution (~ 100 nm) profiles of ozonesondes
291 are interpolated onto OMI retrieval grids (~ 2.5 km thick). We limit OMI/ozonesonde comparisons to OMI
292 solar zenith angle $< 85^\circ$, effective cloud fraction < 0.4 , surface albedo $< 20\%$ (100 %) in tropics and mid-
293 latitudes (high latitude), top altitude of ozonesondes > 30 km, ozonesonde correction factors ranging from
294 0.85 to 1.15 if they exist, and data gaps for each ozonesonde no greater than 3km. Comparisons between
295 OMI and ozonesondes are performed for the tropospheric ozone columns (TCOs) over 3 different latitude
296 bands and for ozone profiles including all the sites, with and without PAs (zero-order) for standard and
297 super Gaussian slit function changes, respectively.

298 In Table 1, the comparison statistics of tropospheric ozone columns between OMI and ozonesonde are
299 summarized as a function of latitude bands. Without using PAs, the comparison results show a noticeable
300 discrepancy in mean biases (1.3-2.1 DU or 3.9-6.4%) due to different assumptions on the slit function shape,
301 with positive biases of 0.3-0.7 DU for super Gaussians and negative biases of 1.0-1.4 DU for standard
302 Gaussians. Overall, OMI retrievals are in a better agreement with ozonesonde measurements using super
303 Gaussians. The correlations and standard deviations are very similar in the tropics and mid-latitudes, but
304 the retrievals with standard Gaussians show better correlation and smaller standard deviations at high-
305 latitudes. As in Sun et al. (2017), the retrievals show significant differences between using standard and
306 super Gaussians, although there are some inconsistencies in comparing OMI and ozonesondes; the main
307 inconsistent factors are: In this study, soft calibration is turned on and a priori information is taken from the
308 TB climatology to perform OMI ozone profile retrievals, whereas soft calibration is turned off and a priori

309 information is taken from the LLM climatology in Sun et al. (2017). OMI/ozonesonde data filtering criteria
310 are quite similar to each other, except that the criteria of the solar zenith angle and cloud fraction are relaxed
311 from 75° and 0.3 to 85° and 0.4, respectively, and the adjustment of ozonesondes with correction factors
312 given for the WOUDC dataset is turned on in this study. Comparison is performed by latitudes here whereas
313 global comparison is analyzed in Sun et al. (2017). After accounting for the slit differences between
314 radiances and irradiances using PAs, the retrievals are improved for both standard and super Gaussians and
315 these two retrievals become consistent except for the use of super Gaussians in the tropics. The mean biases
316 in the tropics and mid-latitudes are almost eliminated, but the standard deviations and correlation do not
317 change much. In the high-latitudes, the standard deviations and correlation are significantly improved due
318 to applying PAs with super Gaussian ISRFs. The lack of improvement with PAs in the tropics with super
319 Gaussians illustrates that ISRFs of radiances are quite similar to those of irradiances in the tropics, while
320 super Gaussians better parameterize OMI ISRFs than standard Gaussians. This is consistent with the
321 comparison of the fitting accuracy of the UV2 band as shown in Figure 7, where the fitting residuals are
322 slightly reduced in the tropics when super Gaussians are linearized, but the standard Gaussian linearization
323 significantly improves the fitting accuracy. The mean biases of the profile comparison as shown in Figure
324 9 clearly show that including PAs to account for ISRF differences reduces mean biases by up to ~ 5 %
325 below 10 km and their general altitude dependence, and improves the consistency between using standard
326 and super Gaussians; in addition, the standard deviations are slightly improved in the 10-20 km altitude
327 range for both Gaussians. The improvement at all latitudes corroborates the change of ISRFs between
328 radiance and irradiance along the orbit as conjectured by Sun et al. (2017). The consistency between using
329 standard and super Gaussians after using PAs is mainly because there is strong anti-correlation between the
330 slit width and shape partial derivatives as shown in Figure 2, so the adjustment of slit width only in the use
331 of standard Gaussians can achieve almost the same effect as the adjustment of both parameters in the use
332 of super Gaussians. Accounting for the wavelength dependent change of the ISRFs with first-order PAs
333 makes insignificant differences to both fit residuals and ozone retrievals (not shown here). This could be
334 mainly explained by the fact of negligible wavelength dependence of OMI ISRFs especially in UV2 as
335 shown in Figure 5, where the PA spectrum ($\frac{\partial \ln I}{\partial p} \cdot \Delta p$) shows almost no variance except at the upper
336 boundary of UV1, as well as in Figure 6 where the UV2 slit parameters derived from irradiances in the sub-
337 fit windows vary within 0.05 nm for FWHM and 0.2 for shape factor.

338 **4. Summary**

339 The knowledge of the Instrument Spectral Response Functions (ISRFs) or slit functions is important
340 for ozone profile retrievals from the Hartley and Huggins bands. ISRFs can be measured in the laboratory
341 prior to launch, but they have been typically derived from solar irradiance measurements assuming

342 Gaussian-like functions in order to account for the effect of the ISRF changes after launch. However, the
343 parameterization of the ISRFs from solar irradiances could be inadequate for achieving a high accuracy of
344 the fitting residuals as ISRFs in radiances could significantly deviate from those in solar radiances (Beirle
345 et al., 2017) and might affect ozone profile retrievals as suggested in Sun et al. (2017). Therefore, this study
346 implements a linearization scheme to account for the spectral errors caused by the ISRF changes as Pseudo
347 Absorbers (PAs) in an optimal estimation based fitting procedure for retrieving ozone profiles from OMI
348 BUUV measurements using the SAO ozone profile algorithm. The ISRFs are assumed to be the generic super
349 Gaussian that can be used as standard Gaussian when fixing the shape factor to 2. This linearization was
350 originally introduced in Beirle et al. (2017) for DOAS analysis, but this study extends this application and
351 more detail how to implement in practice using two different approaches to derive radiance errors from slit
352 function partial derivatives with respect to slit parameters. These two approaches correspond to the two
353 methods of simulating radiances at instrument spectral resolution, one using effective cross sections which
354 were previously used in the SAO ozone profile algorithm and are still used in most of the trace gas retrievals
355 from the UV and visible, and the other calculating radiances at high resolution before convolution, which
356 is the preferred method in the SAO ozone profile algorithm. Consistent PAs are derived with these two
357 approaches, as expected.

358 The fitting coefficients (Δp) to the PAs, representing the difference of slit parameters between radiance
359 and irradiance, are iteratively fitted as part of the state vector along with ozone and other parameters. The
360 UV1 slit parameters show distinct cross-track-dependent differences, especially in high latitudes. In
361 addition, an abnormal Δp caused by scene heterogeneity is observed around bright surfaces and cloudy
362 scenes. The PA spectrum ($\frac{\partial I}{\partial p} \cdot \Delta p$) illustrates that the slit width change causes most of the spectral
363 structures in the UV1 band because the OMI ISRFs are close to Gaussian. Otherwise, the ISRF change
364 results into different spectral responses in the UV2 band with different Gaussian functions because the
365 adjustment of the shape factor becomes more important in accounting for the convolution error when using
366 super Gaussians.

367 Insignificant wavelength dependence on OMI slit functions is demonstrated from slit function
368 parameters derived from irradiances in the sub-fit window, which leads to little difference in ozone profile
369 retrievals when zero and first-order wavelength dependent PA coefficients are implemented to fit the
370 spectral structures caused by slit function errors, respectively. Therefore we evaluate the benefit of
371 including the zero-order PAs fit on both the accuracy of the fitting residuals and the quality of retrieved
372 ozone profiles through validation against ozonesonde observations. Some spikes in the fitting residuals are
373 reduced or eliminated. Commonly, including PAs makes little change on both fit residuals and ozone
374 retrievals in the tropics if super Gaussians are assumed as ISRFs but this is not the case for the standard

375 Gaussian assumption. In the TCO comparison between OMI and ozonesonde, the mean biases are reduced
376 by 0.2 (0.6) DU and 0.6 (1.4) DU in the tropics (mid-latitude) when super and standard Gaussians are
377 linearized, respectively. In particular, applying PA improves the standard deviations at high latitudes by 1.0
378 DU for super Gaussian and 0.5 DU for standard Gaussian. The profile comparison generally shows
379 improvements in mean biases (~ 5% in the lower troposphere) as well as in standard deviation, slightly in
380 the altitude range 10-20 km by applying PAs. More importantly, using these PAs make the retrieval
381 consistent between standard and super Gaussians. Such consistency is due to the anti-correlation between
382 slit width and shape PAs. This study demonstrates the slit function differences between radiance and
383 irradiance and their usefulness to account for such differences on a pixel-to-pixel basis. In this experiment,
384 the soft spectrum, derived with the standard Gaussian assumption, is applied to remove systematic
385 measurement errors before spectral fitting, indicating that the evaluation of ozone retrievals might be
386 unfairly performed for the super Gaussian function implementation. Nonetheless, OMI ozone profile
387 retrievals show better agreement with ozonesonde observations when the super Gaussian is linearized.
388 Actually, the fitting residuals are slightly more broadly structured with super Gaussians than with standard
389 Gaussians if the soft-calibration and PAs are turned off, indicating the benefit of deriving a soft calibration
390 with the super Gaussians. Therefore, there is still room for achieving better benefits when using the PAs on
391 ozone profile retrievals by applying the soft calibration derived with super Gaussians.

392

393 *Author contributions.* JB and XL designed the research; XL provided oversight and guidance; KC and JB
394 developed the methodology together; JB conducted the research and wrote the paper; XL, SK, KC, and
395 JHK contributed to the analysis and writing.

396 *Competing interests.* The authors declare that they have no conflict of interest.

397

398

Acknowledgements

399 We acknowledge the OMI science team for providing their satellite data and the WOUDC and SHADOZ
400 networks for their ozonesonde datasets. Research at the Smithsonian Astrophysical Observatory by J. Bak,
401 X. Liu, K. Sun, and K. Chance was funded by NASA Aura science team program (NNX14AF16G &
402 NNX17AI82G). Research at Pusan National University by J. H Kim was supported by the Korea Ministry
403 of Environment (MOE) as the Public Technology Program based on Environmental Policy
404 (2017000160001).

405

406

407

408

References

409

410 Azam, F. and Richter, A.: GOME2 on MetOp: Follow on analysis of GOME2 in orbit degradation, Final
411 report, EUM/CO/09/4600000696/RM, 2015, available at: [http://www.doas-](http://www.doas-bremen.de/reports/gome2_degradation_follow_up_final_report.pdf)
412 [bremen.de/reports/gome2_degradation_follow_up_final_report.pdf](http://www.doas-bremen.de/reports/gome2_degradation_follow_up_final_report.pdf) (last access: 7 September 2016),
413 2015.

414 Bak, J., Liu, X., Wei, J. C., Pan, L. L., Chance, K., and Kim, J. H.: Improvement of OMI ozone profile
415 retrievals in the upper troposphere and lower stratosphere by the use of a tropopause-based ozone profile
416 climatology, *Atmos. Meas. Tech.*, 6, 2239–2254, doi:10.5194/amt-6-2239-2013, 2013.

417 Bak, J., Liu, X., Kim, J.-H., Haffner, D. P., Chance, K., Yang, K., and Sun, K.: Characterization and
418 correction of OMPS nadir mapper measurements for ozone profile retrievals, *Atmos. Meas. Tech.*, 10,
419 4373-4388, <https://doi.org/10.5194/amt-10-4373-2017>, 2017.

420 Beirle, S., Sihler, H., and Wagner, T.: Linearisation of the effects of spectral shift and stretch in DOAS
421 analysis, *Atmos. Meas. Tech.*, 6, 661–675, doi:10.5194/amt-6-661-2013, 2013.

422 Beirle, S., Lampel, J., Lerot, C., Sihler, H., and Wagner, T.: Parameterizing the instrumental spectral
423 response function and its changes by a super-Gaussian and its derivatives, *Atmos. Meas. Tech.*, 10, 581-
424 598, <https://doi.org/10.5194/amt-10-581-2017>, 2017.

425 Brion, J., Chakir, A., D. Daumont, D., and Malicet, J.: High-resolution laboratory absorption cross section
426 of O₃. Temperature effect, *Chem. Phys. Lett.*, 213(5–6), 610– 612, 1993.

427 Cai, Z., Liu, Y., Liu, X., Chance, K., Nowlan, C. R., Lang, R., Munro, R., and Suleiman, R.: ,
428 Characterization and correction of Global Ozone Monitoring Experiment 2 ultraviolet measurements
429 and application to ozone profile retrievals, *J. Geophys. Res.*, 117, D07305, doi:10.1029/2011JD017096,
430 2012.

431 Caspar, C. and Chance, K.: GOME wavelength calibration using solar and atmospheric spectra, Third ERS
432 Symposium on Space at the Service of our Environment, Florence, Italy, 14–21 March, 1997.

433 Dobber, M., Voors, R., Dirksen, R., Kleipool, Q., and Levelt, P.: The high-resolution solar reference
434 spectrum between 250 and 550 nm and its application to measurements with the Ozone Monitoring
435 Instrument, *Solar Physics*, 249, 281–291, 2008. Kim, P. S., Jacob, D. J., Liu, X., Warner, J. X., Yang,
436 K., Chance, K., Thouret, V., and Nedelec, P.: Global ozone–CO correlations from OMI and AIRS:
437 constraints on tropospheric ozone sources, *Atmos. Chem. Phys.*, 13, 9321-9335,
438 <https://doi.org/10.5194/acp-13-9321-2013>, 2013.

439 Fu, D., Worden, J. R., Liu, X., Kulawik, S. S., Bowman, K. W., and Natraj, V.: Characterization of ozone
440 profiles derived from Aura TES and OMI radiances, *Atmos. Chem. Phys.*, 13, 3445-3462,
441 <https://doi.org/10.5194/acp-13-3445-2013>, 2013. Kim, P. S., Jacob, D. J., Liu, X., Warner, J. X., Yang,
442 K., Chance, K., Thouret, V., and Nedelec, P.: Global ozone–CO correlations from OMI and AIRS:
443 constraints on tropospheric ozone sources, *Atmos. Chem. Phys.*, 13, 9321-9335,
444 <https://doi.org/10.5194/acp-13-9321-2013>, 2013.

445 Fu, D., Kulawik, S. S., Miyazaki, K., Bowman, K. W., Worden, J. R., Eldering, A., Livesey, N. J., Teixeira,
446 J., Irion, F. W., Herman, R. L., Osterman, G. B., Liu, X., Levelt, P. F., Thompson, A. M., and Luo, M.:
447 Retrievals of tropospheric ozone profiles from the synergism of AIRS and OMI: methodology and
448 validation, *Atmos. Meas. Tech.*, 11, 5587-5605, <https://doi.org/10.5194/amt-11-5587-2018>, 2018.

449 Kroon, M., de Haan, J. F., Veefkind, J. P., Froidevaux, L., Wang, R., Kivi, R., and Hakkarainen, J. J.:
450 Validation of operational ozone profiles from the Ozone Monitoring Instrument, *J. Geophys. Res.*, 116,
451 D18305, doi:10.1029/2010JD015100, 2011.

452 Levelt, P. F., van den Oord, G. H. J., Dobber, M. R., Malkki, A., Visser, H., de Vries, J., Stammes, P.,
453 Lundell, J. O. V., and Saari, H.: The ozone monitoring instrument, *IEEE Transactions on Geoscience
454 and Remote Sensing*, 44, 1093–1101, doi:10.1109/TGRS.2006.872333, 2006.

455 Liu, X., Chance, K., Sioris, C. E., Spurr, R. J. D., Kurosu, T. P., Martin, R. V., and Newchurch, M. J.:
456 Ozone profile and tropospheric ozone retrievals from Global Ozone Monitoring Experiment: algorithm
457 description and validation, *J. Geophys. Res.*, 110, D20307, doi: 10.1029/2005JD006240, 2005.

458 Liu, X., Bhartia, P.K, Chance, K, Spurr, R.J.D., and Kurosu, T.P.: Ozone profile retrievals from the ozone
459 monitoring instrument. *Atmos. Chem. Phys.*, 10, 2521–2537, 2010.

460 Liu, C., Liu, X., Kowalewski, M.G., Janz, S.J., González Abad, G., Pickering, K.E., Chance, K., and
461 Lamsal, L.N.: Characterization and verification of ACAM slit functions for trace gas retrievals during
462 the 2011 DISCOVER-AQ flight campaign, *Atmos. Meas. Tech.*, 8, 751-759, doi:10.5194/amt-8-751-
463 2015, 2015.

464 Mielonen, T., de Haan, J. F., van Peet, J. C. A., Eremenko, M., and Veefkind, J. P.: Towards the retrieval
465 of tropospheric ozone with the Ozone Monitoring Instrument (OMI), *Atmos. Meas. Tech.*, 8, 671-687,
466 <https://doi.org/10.5194/amt-8-671-2015>, 2015.

467 Schenkeveld, V. M. E., Jaross, G., Marchenko, S., Haffner, D., Kleipool, Q. L., Rozemeijer, N. C., Veefkind,
468 J. P., and Levelt, P. F.: In-flight performance of the Ozone Monitoring Instrument, *Atmos. Meas. Tech.*,
469 10, 1957-1986, <https://doi.org/10.5194/amt-10-1957-2017>, 2017.

470 Sioris, C. E. and Evans, W. F. J.: Impact of rotational Raman scattering in the O₂ A band, *Geophys. Res.
471 Lett.*, 27, 4085–4088, 2000.

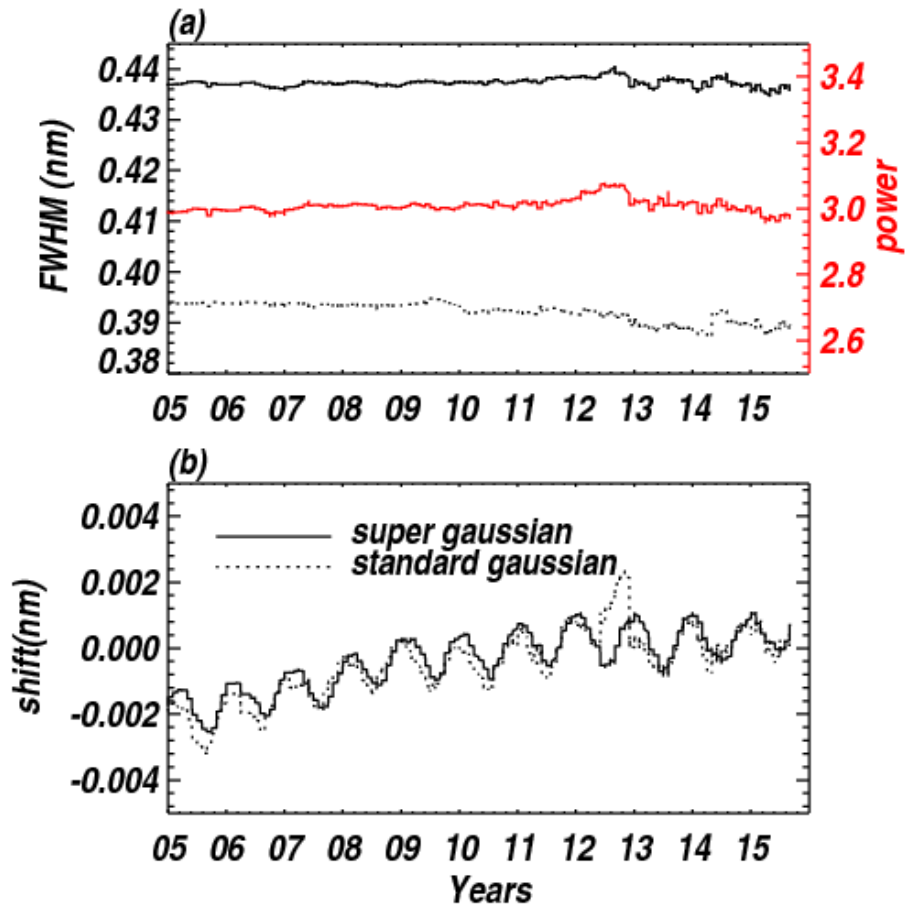
472 Spurr, R. J. D.: Linearized pseudo-spherical scalar and vector discrete ordinate radiative transfer models
473 for use in remote sensing retrieval problems, in: *Light Scattering Reviews*, edited by: Kokhanovsky, A.,
474 Springer, New York, 2008.

475 Sun, K., Liu, X., Huang, G., González Abad, G., Cai, Z., Chance, K., and Yang, K.: Deriving the slit
476 functions from OMI solar observations and its implications for ozone-profile retrieval, *Atmos. Meas.
477 Tech.*, 10, 3677-3695, <https://doi.org/10.5194/amt-10-3677-2017>, 2017.

478 van Hees, R. M., Tol, P. J. J., Cadot, S., Krijger, M., Persijn, S. T., van Kempen, T. A., Snel, R., Aben, I.,
479 and Hoogeveen, Ruud W. M.: Determination of the TROPOMI-SWIR instrument spectral response
480 function, *Atmos. Meas. Tech.*, 11, 3917-3933, <https://doi.org/10.5194/amt-11-3917-2018>, 2018.

481 Wilmoth, D. M., Hanisco, T. F., Donahue, N. M., and Anderson, J. G.: Fourier transform ultraviolet
482 spectroscopy of the $A^2\Pi_{3/2} - X^2\Pi_{3/2}$ Transition of BrO, *J. Phys. Chem. A.*, 103(45), 8935– 8945, 1999.

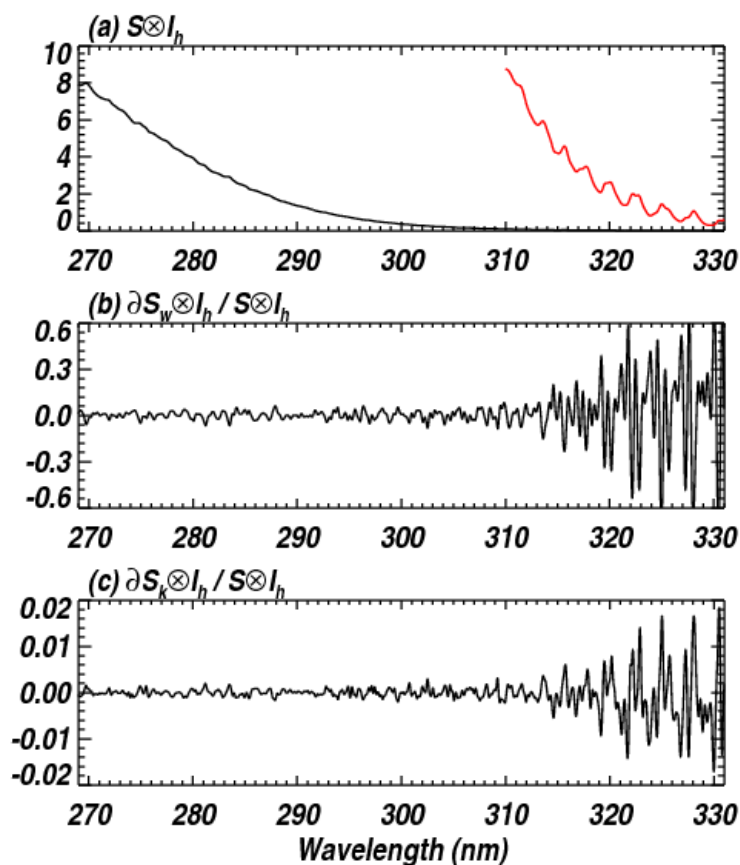
483



484

485

486 Figure 1. Time series of (a) slit parameters and (b) wavelength shifts for OMI daily irradiance
 487 measurements (310-330 nm) at nadir cross track position when super Gaussians (solid line) and
 488 standard Gaussians (dotted line) are parameterized as slit function shapes, respectively.



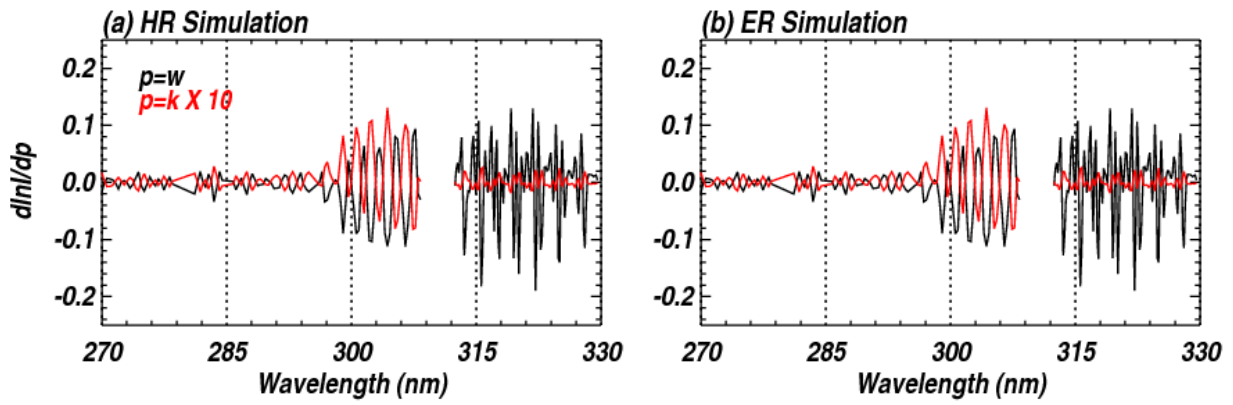
490

491 **Figure 2. (a) Ozone absorption cross sections ($\text{cm}^2/\text{molecule}$) (δ_h) at different scales (red and black) at**
 492 **a representative temperature (238.12 K) calculated via convolution of high-resolution (0.01 nm)**
 493 **reference spectrum with the super Gaussian slit function, S ($k = 2.6, w = 0.26$ nm). (b) and (c) its**
 494 **derivatives with respect to slit parameters ($\partial S_p = \frac{\partial S}{\partial p}$), w and k , respectively, normalized to the**
 495 **convolved cross sections.**

496

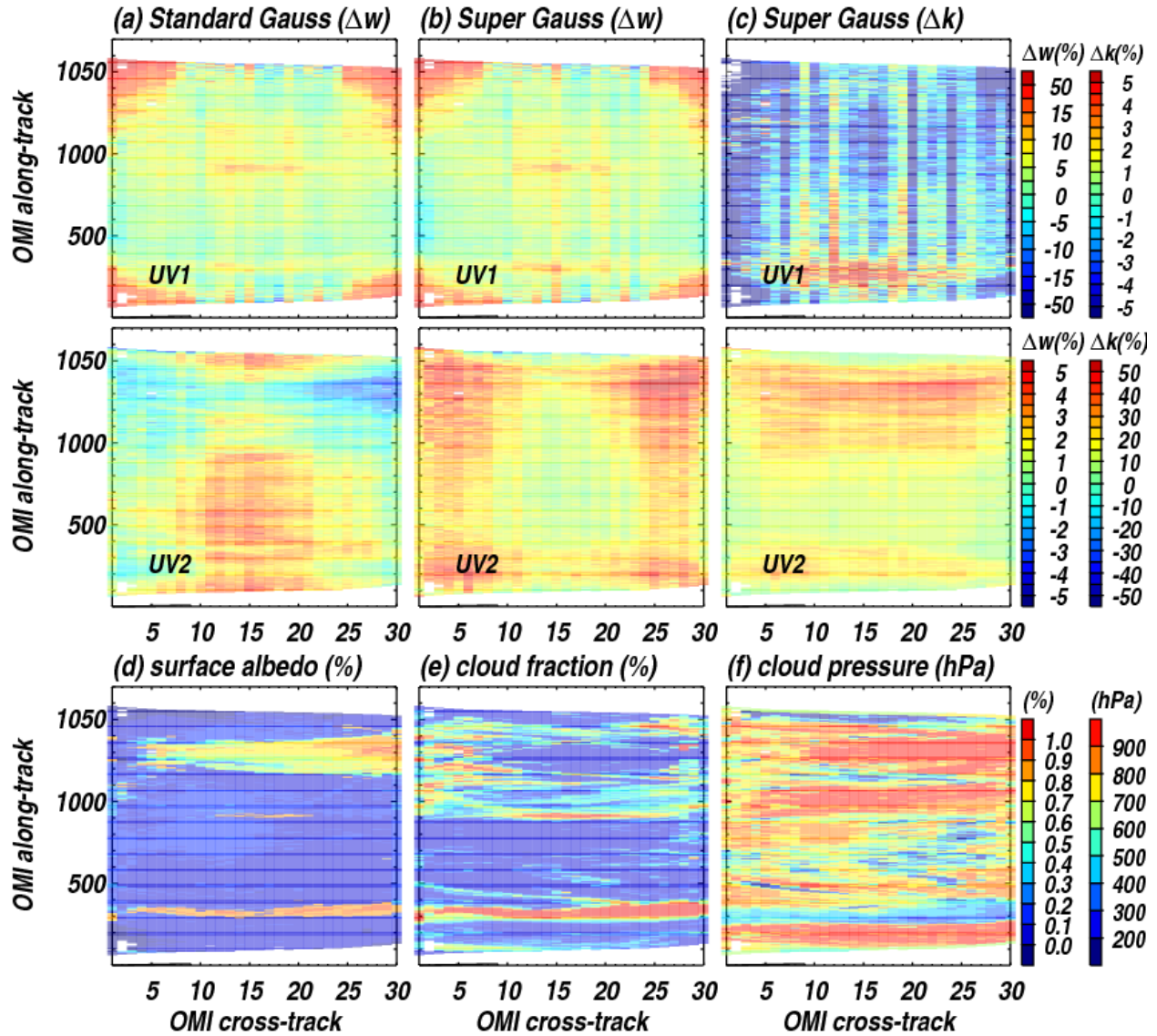
497

498



499

500 Figure 3. Derivatives of an OMI radiance spectrum simulated using high-resolution (HR) and effective
 501 resolution (ER) cross section spectra with respect to slit parameters assuming a super Gaussian function.
 502 $d\ln I/dk$ is multiplied by a factor of 10 to visually match $d\ln I/dw$ on the same y-axis.



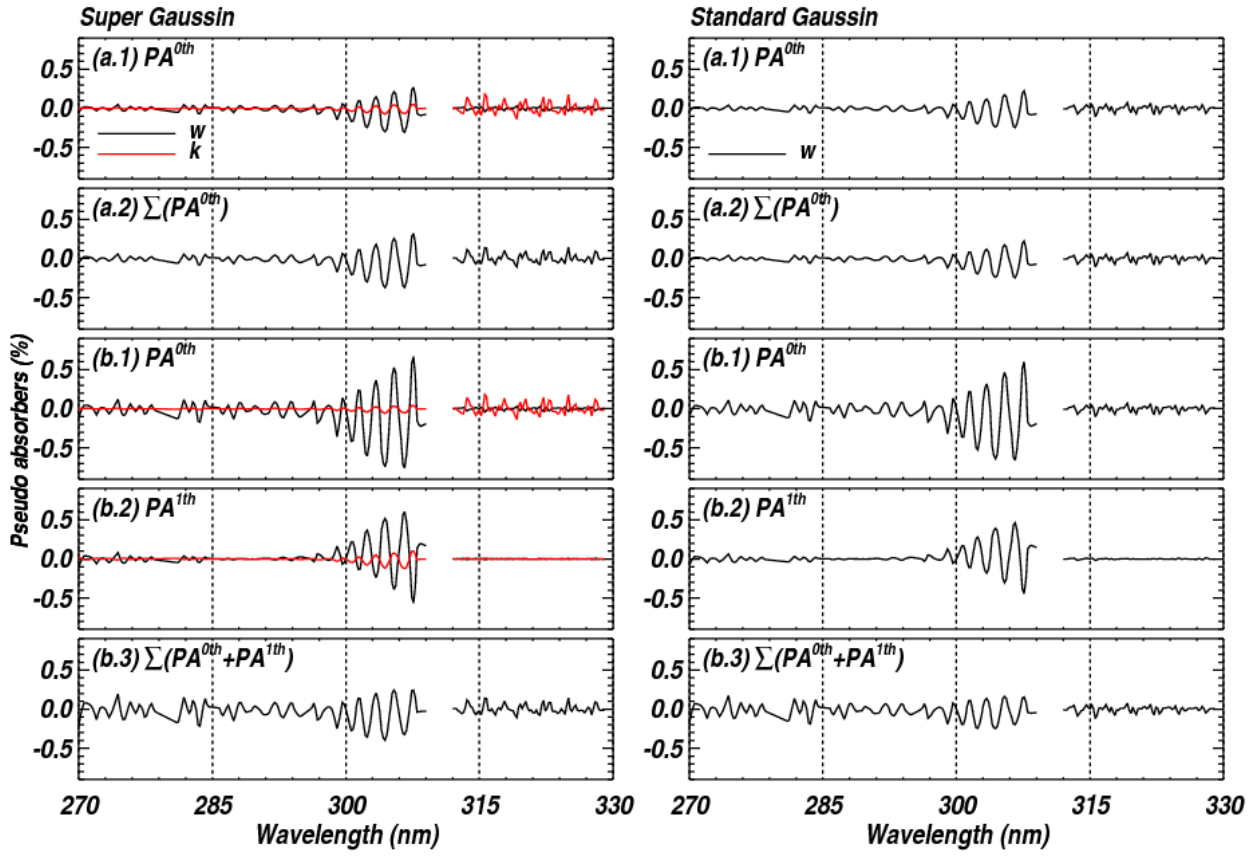
503

504 Figure 4. Pseudo absorption coefficients (Δw , Δk) for fitting OMI radiances to account for slit function
 505 changes assuming (a) standard Gaussian and (b-c) super Gaussian, for the first orbit of measurements
 506 on 1 July 2006, with (d-f) the corresponding geophysical parameters. Δw and Δk are displayed after
 507 being normalized with w_o , and k_o , the slit parameters derived from OMI solar irradiance
 508 measurements.

509

510

511



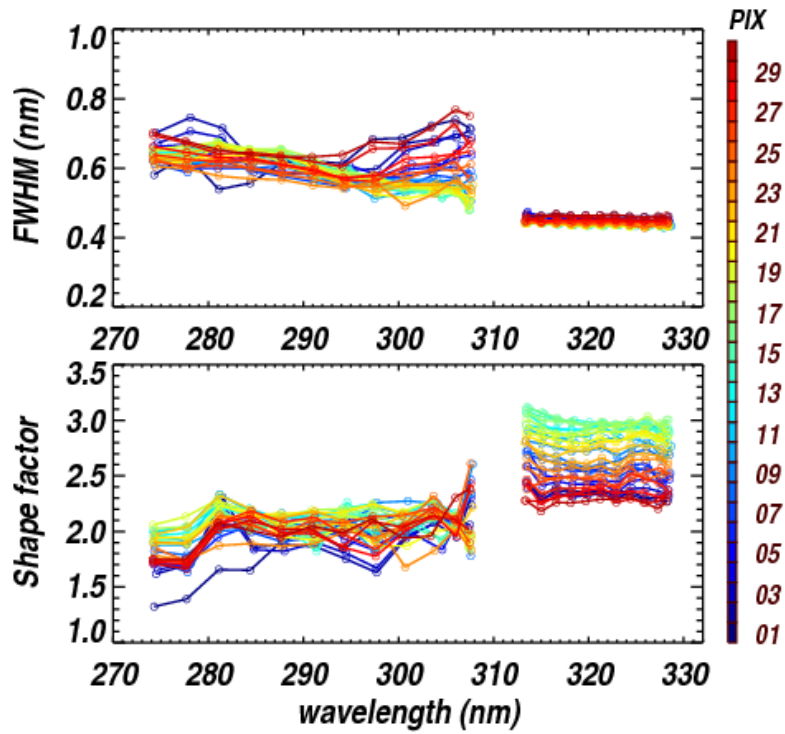
512

513 Figure 5. (a.1) Pseudo absorber spectra multiplied by corresponding zero order coefficients, $\frac{\partial \ln I}{\partial p} \times \Delta p_o$
 514 and (a.2) the sum of them for (left) super Gaussian and (right) standard Gaussian function
 515 parameterizations, respectively. (b) is same as (a), but for first order polynomial coefficients, $\frac{\partial \ln I}{\partial p} \times$
 516 $\Delta p_i (\lambda - \bar{\lambda})^i (i = 0,1)$. This example represents an average at nadir in the latitude zone 30°-60°N from
 517 measurements used in Figure 4.

518

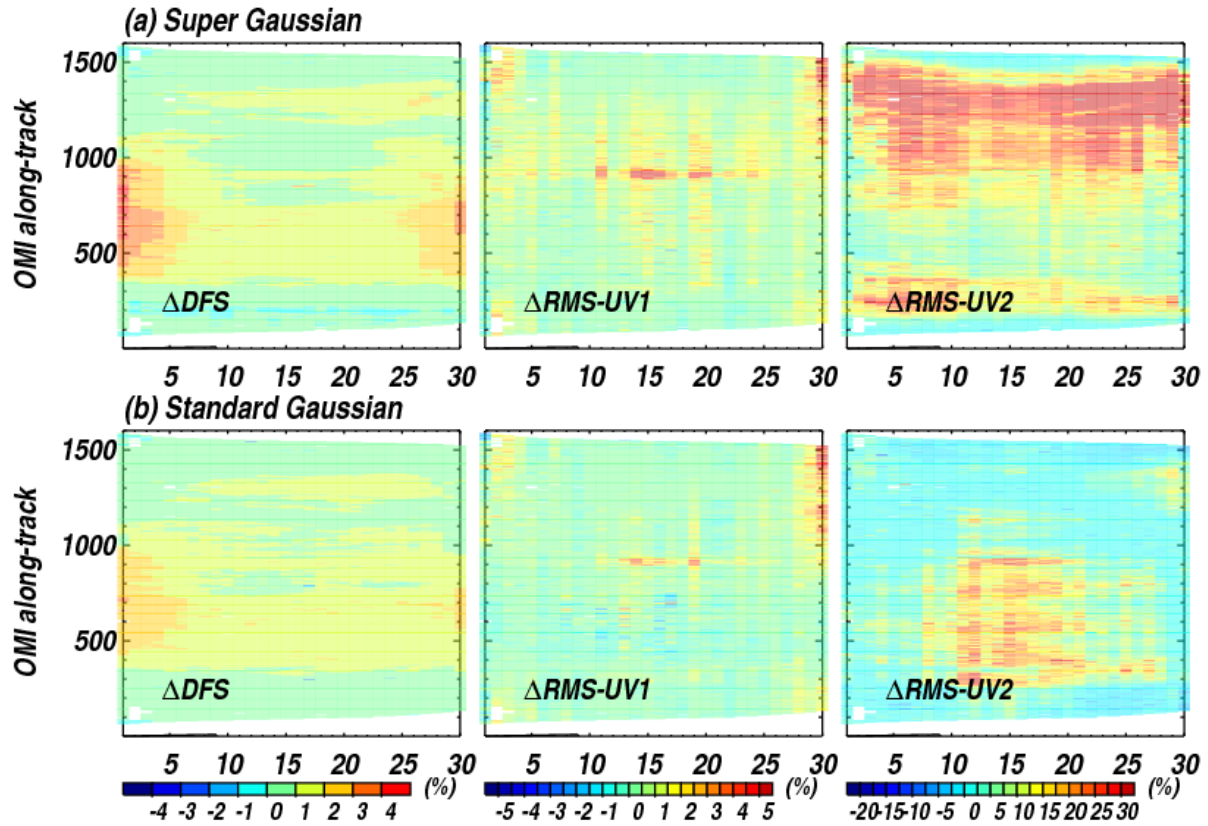
519

520



521

522 Figure 6. OMI ISRF FWHM (nm) and shape factor (k) as functions of the center wavelength, as derived
 523 from OMI solar irradiances assuming Super Gaussian functions over a range of 31 spectral pixels in 10-
 524 pixel increments. Different colors represent different cross-track positions from 1 (blue) to 30 (red).



525

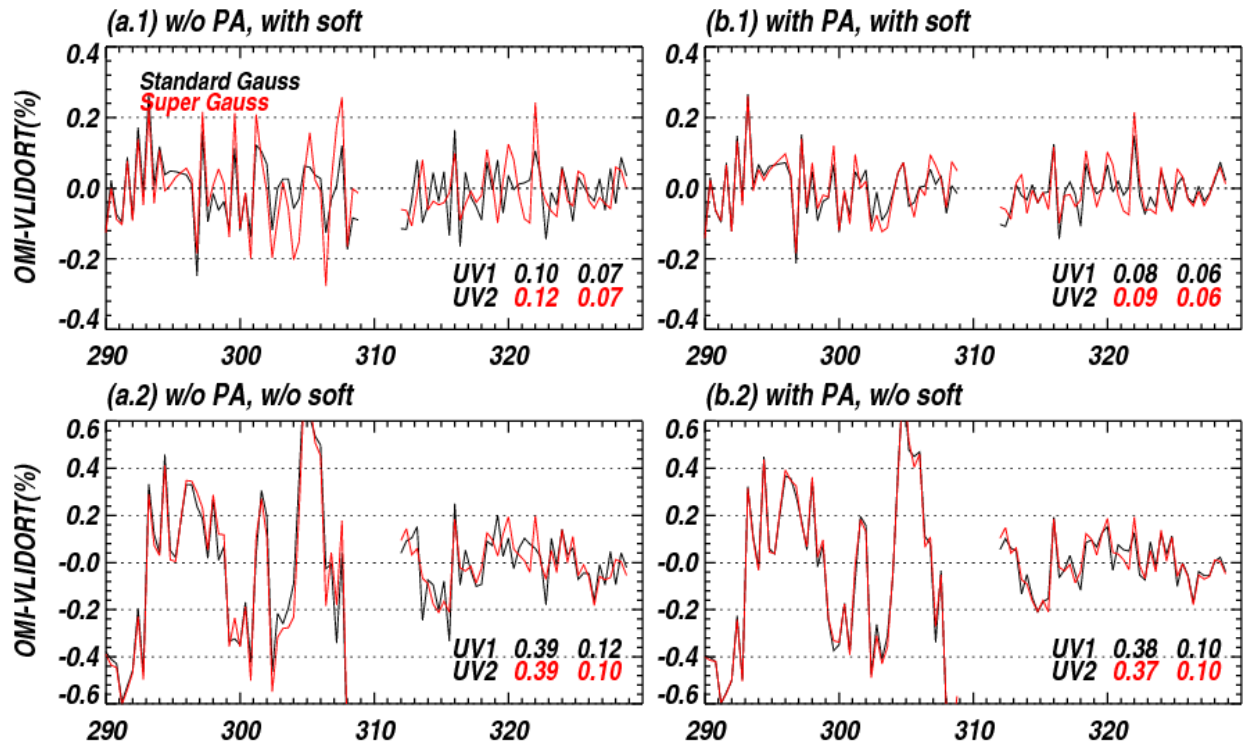
526 Figure 7. Same as Figure 4, but for comparisons of the Degrees of Freedom for Signal (DFS) and the Root
 527 Mean Square (RMS) of spectral fitting residuals in UV 1 and UV2 with and without zero-order pseudo
 528 absorber. Positive values indicate that both fitting residuals and DFSs are reduced due to the pseudo
 529 absorber.

530

531

532

533



534

535

536 **Figure 8. Average differences (%) between measured (OMI) and simulated (VLIDORT) radiances at the**
 537 **nadir cross-track pixel in the tropics (30°S-30°S) from measurements used in Figure 4, without (a) and**
 538 **with (b) zero-order pseudo absorbers (PA) when the standard Gaussian (black line) and the super**
 539 **Gaussian (red line) are assumed as ISRFs, respectively. Upper/lower panels represent the fitting results**
 540 **with soft calibration being turned on/off. The residuals in the UV1 (< 310 nm) are scaled by a factor of 2**
 541 **to fit in the given y-axis. In the legend, the RMS of residuals (%) are given for UV1 and UV2 wavelength**
 542 **ranges, respectively.**

543

544

545

546

547

548

549

550

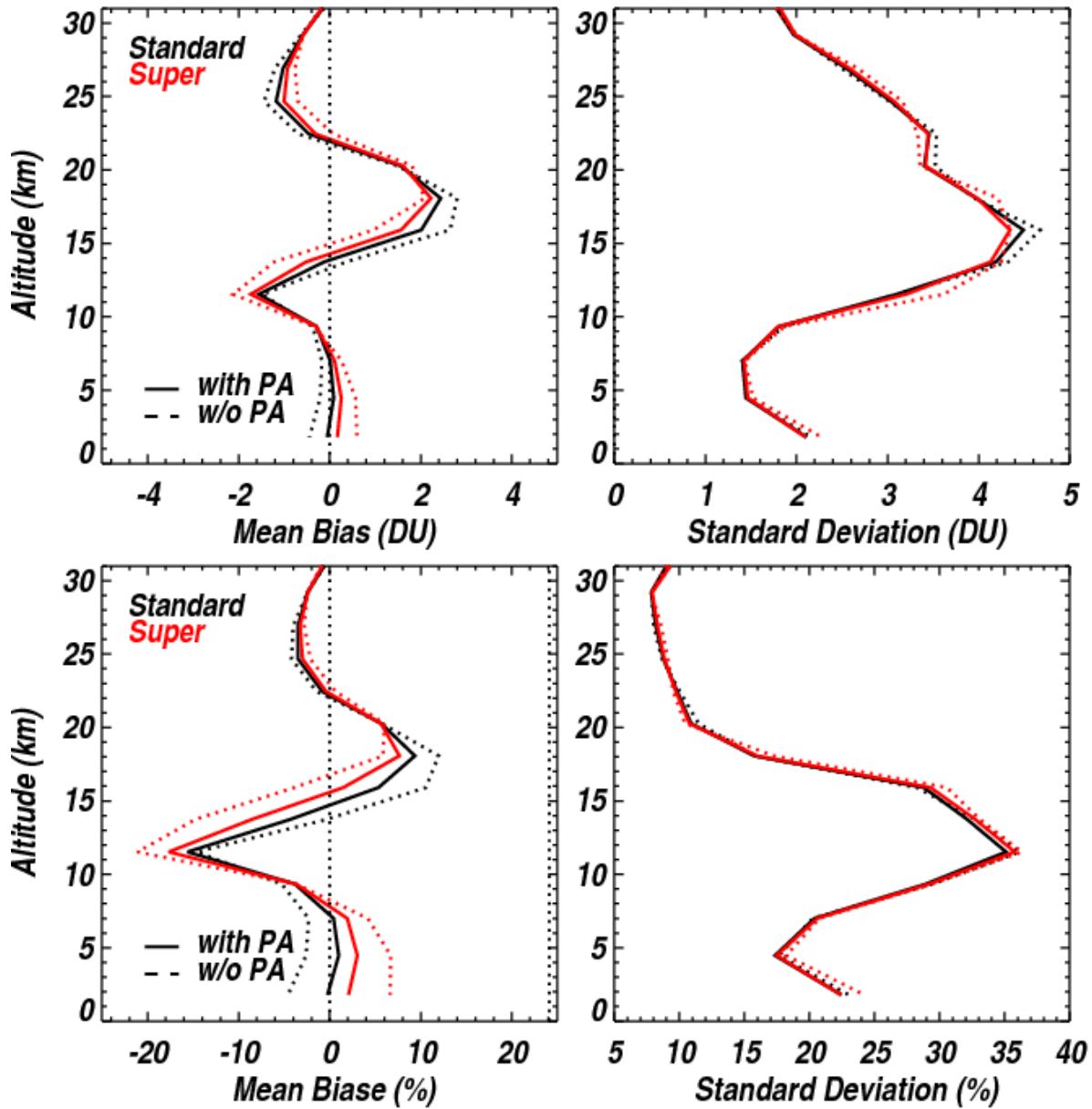
551

552

553 **Table 1. Comparison Statistics (Mean Bias in DU/%, 1 σ Standard Deviation in DU/%, the Pearson**
 554 **Correlation Coefficient, number of collocations) of OMI and ozonesonde tropospheric column ozone**
 555 **from 2005 to 2008 over (a) tropical, (b) midlatitude, and (c) high-latitude stations.**

(a) Tropics (30°S-30°N)			
Super Gaussian		Standard Gaussian	
With PA	w/o PA	With PA	w/o PA
-0.1±5.1DU (-0.3±15.8%) R=0.82, N=580	0.3±4.9DU (0.8±15.5%) R=0.83, N= 580	-0.4±5.3DU (-1.2±16.3%) R=0.81, N=582	-1.0±5.1DU (-3.1±16.0%) R=0.83, N=579
(b) Midlatitude (30°N-60°N)			
Super Gaussian		Standard Gaussian	
With PA	w/o PA	With PA	w/o PA
-0.1±4.9DU (0.0±14.5%) R=0.83, N=2336	0.7±5.0DU (2.3±15.0%) R=0.82, N=2333	0.0±5.0DU (0.3±15.0%) R=0.82, N=2315	-1.4±4.9DU (-4.1±14.6%) R=0.83, N=2317
(c) High-latitude (60°N-90°N)			
Super Gaussian		Standard Gaussian	
With PA	w/o PA	With PA	w/o PA
-0.7±5.2DU (-2.1±18.4%) R=0.61, N=447	0.3±6.2DU (1.5±22.2%) R=0.53, N=448	-0.6±4.9DU (-1.7±17.1%) R=0.65, N=433	-1.0±5.4DU (-3.2±18.7%) R=0.60, N=433

556



557

558 Figure 9. Same as Table 1, but for global mean biases and 1σ standard deviations of the differences
 559 between OMI and ozonesondes at each OMI layer, with different slit function
 560 assumptions/implementations. The absolute and relative differences are used in the upper and lower
 561 comparisons, respectively.

562

563

564

565